

## Article

# Fracture Analysis of Ultrahigh-Strength Steel Based on Split Hopkinson Pressure Bar Test

Shihong Xiao <sup>1,2</sup>, Xiaosheng Luan <sup>1</sup>, Zhiqiang Liang <sup>1,\*</sup> , Xibin Wang <sup>1</sup>, Tianfeng Zhou <sup>1</sup> and Yue Ding <sup>2</sup>

<sup>1</sup> School of Mechanical Engineering, Beijing Institute of Technology, Beijing 100081, China; xiaoshih@126.com (S.X.); 3120185213@bit.edu.cn (X.L.); cutting0@bit.edu.cn (X.W.); zhoutf@bit.edu.cn (T.Z.)

<sup>2</sup> AVIC Manufacturing Technology Institute, Beijing 100024, China; dingyue105@163.com

\* Correspondence: liangzhiqiang@bit.edu.cn; Fax: +86-10-6891-1717

**Abstract:** Impact loading is an important cause of fracture failure of ultrahigh-strength steel parts during service. Revealing the fracture mechanism of ultrahigh-strength steel under impact loading has important reference significance for the material preparation, part design, and manufacturing of such steel. Based on the split Hopkinson pressure bar (SHPB) test, the mechanical response characteristics of 45CrNiMoVA steel under impact loading were analyzed, and the true stress–true strain curves under a high strain rate ( $10^3 \text{ s}^{-1}$ ) were obtained. It was found that under the simultaneous action of forward and tangential loading forces, a severe plastic deformation layer with a thickness of 20–30  $\mu\text{m}$  was generated in the near impact-loading end face, which is the main cause for crack initiation and propagation. Under the condition of a high strain rate, the plastic flow stress of 45CrNiMoVA steel was characterized by the equilibrium of strain hardening and strain softening, and its impact fracture toughness decreased by 43.6%, resulting in increased quasi-cleavage fracture. Hence, severe surface plastic deformation during 45CrNiMoVA steel machining should be avoided, as it may lead to early failure.



**Citation:** Xiao, S.; Luan, X.; Liang, Z.; Wang, X.; Zhou, T.; Ding, Y. Fracture Analysis of Ultrahigh-Strength Steel Based on Split Hopkinson Pressure Bar Test. *Metals* **2022**, *12*, 628. <https://doi.org/10.3390/met12040628>

Academic Editors: Zhenjia Xie, Xueda Li and Xiangliang Wan

Received: 22 February 2022

Accepted: 30 March 2022

Published: 6 April 2022

**Publisher's Note:** MDPI stays neutral with regard to jurisdictional claims in published maps and institutional affiliations.



**Copyright:** © 2022 by the authors. Licensee MDPI, Basel, Switzerland. This article is an open access article distributed under the terms and conditions of the Creative Commons Attribution (CC BY) license (<https://creativecommons.org/licenses/by/4.0/>).

**Keywords:** ultrahigh-strength steel; fracture; impact loading; SHPB

## 1. Introduction

Ultrahigh-strength steel is widely used in high-bearing structural parts, such as aircraft landing gear, rotor shafts, and torsion shafts, in diverse fields such as aviation, vehicles, and power generation. These parts are often subjected to impact loading during service. Their service life and failure mode are closely related to the impact load [1–3]. Therefore, revealing the fracture mechanism of ultrahigh-strength steel under impact loading is crucial for the optimization of the structural design and manufacturing process of ultrahigh-strength steel parts.

The study of the mechanical properties under impact loading can be used for the correction-rate-dependent model [4–6]. Qin et al. [7] pointed out that the cause of 45CrNiMoVA gear fracture was insufficient fatigue strength and excessive external impact force. Hu et al. [5] found that the strain hardening and strain rate effect of 45CrNiMoVA material in the process of cutting or impact was different from that in the static state, which cannot be ignored. Rakvåg et al. [8] found that there was a critical impact speed in the change of deformation and the fracture mode of high-strength steel. Under impact loading, the dominant fracture mode of plastic materials was tensile splitting and spiral shearing, while the dominant fracture mode of brittle materials was shear fracture and full fragmentation. Zhang et al. [9,10] posited that the high strain rate in the process of material processing leads to embrittlement and found the “skin effect”, which can improve the processing quality by controlling the strain rate. Sufficient research has shown that material performance under impact loading is abnormal. To ensure the safety of the service process of ultrahigh-strength steel parts, it is important to study the deformation and fracture characteristics

of ultrahigh-strength steel under impact loading for the design of structural parts and the prevention of failure.

Compared with the quasi-static state, the mechanical properties of metal materials change obviously at high strain rates; for example, the yield strength, ultimate strength, and failure strain increase, and the fracture toughness decreases [11,12]. Hu et al. [13] found that Aermet 100 steel had a strong strain rate sensitivity. The yield strength was 1800 MPa under quasi-static compression and 2300 MPa under a strain rate of  $4200 \text{ s}^{-1}$ , which equates to an increase of 24%. Singh et al. [14] found that the yield strength of mild steel had a higher strain rate sensitivity than the ultimate tensile strength. The yield strength at the strain rate  $750 \text{ s}^{-1}$  was 2.5 times that at a quasi-static state. Work hardening, phase transformation, strain aging, and dynamic recrystallization are the main mechanisms of the above changes. Among them, adiabatic shear bands (ASBs) are the most important deformation and fracture mechanism of metal materials at a high strain rate. Ghomi and Odeshi [15] found that the local high-density deformation of martensitic steel under impact loading resulted in the change of the structure and mechanical properties of the ASB, the refinement of grains, and the increase in hardness, which increase the possibility of brittle fracture. Ren et al. [16] found that the ASB is closely related to the plastic strain energy density during the impact deformation of ultrahigh-strength steel 35CrMnSiA. The phase transformation caused by continuous dynamic recrystallization can improve the strength of 35CrMnSiA but weaken its plasticity. Harding et al. [17] found evidence of deformation-induced martensitic transformation in the shear band. Hao et al. [18] found that the failure mechanism of the Ti-47Al-2Cr-2Nb alloy under dynamic compression was brittle shear failure, which propagated rapidly along the lamellar interface and developed into adiabatic shear when the temperature increased. Nesterenko et al. [19] found that the formation of localization on the grain scale under impact loading made the plastic deformation uneven after critical strain, which was caused by texture softening and flow stress anisotropy. Krüger et al. [20] found that the strain rate reduced the martensite transformation rate and strain hardening rate. The change of these mechanical properties under impact loading also reflects the change of deformation and the fracture mechanism. In the technology of ultrasonic rolling deformation strengthening, the principle of ultrasonic-impact, high-strain-rate deformation can lead to grain refinement and improve the fatigue performance of structural parts [21,22].

There are many types of fracture mechanisms (crack propagation), among which fatigue and fracture toughness are important types. Qi et al. [23] attributed the excellent fracture toughness to that in the small plastic deformation area at the crack tip, and strain-induced martensite transformation occurred in the reverse austenite, which absorbed the strain energy, relieved the local stress concentration, and inhibited the crack growth. Research of Das et al. [24] on the damage accumulation of high-strength steel showed that the damage accumulation caused by strain was also highly sensitive to the stress state. The influence of stress on the damage accumulation was greater than that of other variables, and the strain rate was an important factor affecting the damaged area of the hole in the material. Gronostajski et al. [25] studied the microstructure change and flow stress of high-strength steel, considering the transformation of retained austenite to martensite at a high strain rate. They found that in addition to the thermodynamic stability of retained austenite, the higher the temperature, the higher the strain rate of plastic deformation, which would affect the shape of the true stress–true strain curve. Owing to the delayed transformation from austenite to martensite, no tempering of martensite was observed. Compared with austenitic steel, martensitic steel is more sensitive to the strain rate. The fracture analysis of Khodabakhshi et al. [26] showed that with the formation of the martensite phase, the fracture mode changed from ductile fracture to ductile–brittle fracture, and the fracture composition changed from shear to tensile at a high strain rate. Wang et al. [27] described cleavage and micropore growth/coalescence in the fracture process of metal materials. In the process of deformation, the dislocation will be emitted from the crack tip, and then the dislocation will be blocked around the precipitate near the crack tip, resulting in the

formation of microcavities around the precipitate. For materials with high yield strength, the radius of the plastic zone near the crack tip will be extremely small. In this case, the crack tip will not be passivated, and the stress concentration will not be effectively relieved. When the local stress in front of the crack tip exceeds the cleavage fracture strength, the crack tip can be connected with the micro void through cleavage fracture, thus producing the cleavage surface and dimple. Therefore, understanding the deformation and fracture mechanism of ultrahigh-strength steel under impact loading is the main research direction of this paper.

In summary, the mechanical properties, deformation mechanism, crack propagation, and fracture toughness of metal materials under impact loading are different. Failure accidents of ultrahigh-strength steel parts under impact loading are still frequent, and the research on the failure caused by impact load has been valuable. Based on the split Hopkinson pressure bar (SHPB) test, the true stress–true strain curves of 45CrNiMoVA steel under a high strain rate ( $10^3 \text{ s}^{-1}$ ) were obtained, and the deformation, fracture, and failure characteristics under different impact loads were studied. The microstructure, crack propagation, and fracture morphology were detected and analyzed to reveal the failure causes of impact fracture.

## 2. Experiment

### 2.1. Materials of Specimen

The test material was ultrahigh-strength steel 45CrNiMoVA, and its chemical composition is listed in Table 1. It can be obtained from the Chinese national standard GB/T 3077-2015. Table 2 shows the mechanical property parameters of 45CrNiMoVA, as given by Chen et al. [28]. The heat treatment process of the specimen material includes: first heat preservation at 860 °C for 40 min, oil cooling at about 60 °C, heat preservation at 210 °C for about 300 min, and then air cooling. The microstructure was mainly uniform lath tempered martensite with a small amount of retained austenite, as shown in Figure 1a. Based on the Electron Backscatter Diffraction (EBSD) test results, the grain size of lath-tempered martensite was mainly distributed at 0.5–2.5  $\mu\text{m}$ , as shown in Figure 1b.

**Table 1.** Chemical composition of 45CrNiMoVA materials (wt%).

C	Cr	Ni	Mo	V	Si	Mn	S	P
0.42–0.49	0.80–1.1	1.3–1.8	0.20–0.30	0.10–0.20	0.17–0.37	0.50–0.80	$\leq 0.015$	$\leq 0.02$

**Table 2.** Mechanical properties of 45CrNiMoVA material, Data from [28].

Tensile Strength, $\sigma_b$ (MPa)	Yield Strength, $\sigma_{0.2}$ (MPa)	Elastic Modulus, $E$ (GPa)	Elongation, $\delta_5$ (%)	Reduction in Area, $\psi$ (%)	Fracture Toughness, $K_{IC}$ (MPa·m <sup>1/2</sup> )
2120	1639	175	11	27.3	41.8

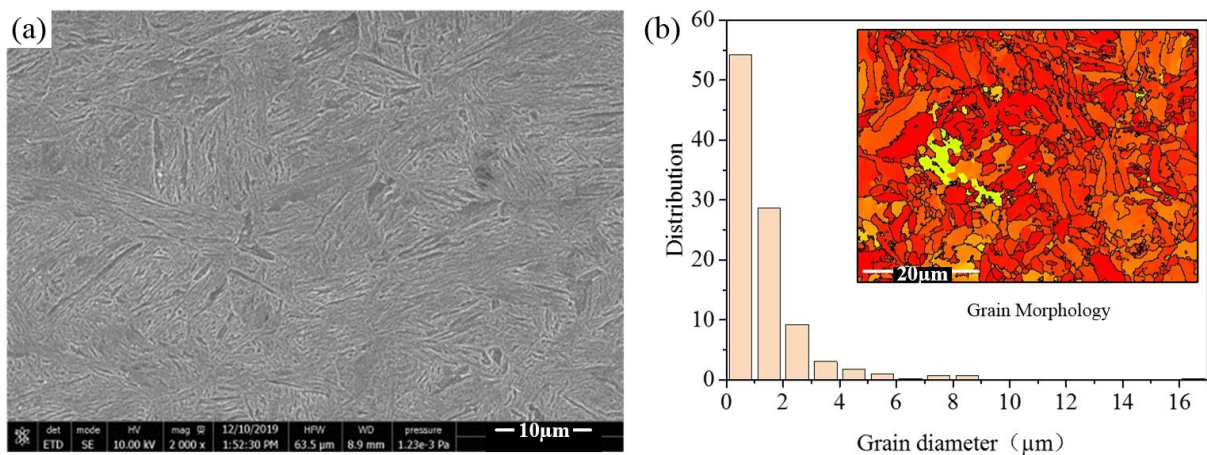


**Figure 1.** (a) Microstructure and morphology of 45CrNiMoVA steel specimen; (b) Grain size distribution of specimen material.

## 2.2. Impact Test Method

SHPB is the main means to test the dynamic mechanical properties of materials at medium and high strain rates ( $10^2 \text{ s}^{-1}$ – $10^4 \text{ s}^{-1}$ ). In this experiment, based on the 5 mm diameter SHPB, the specimens were impacted at different impact speeds (17.2 m/s, 18.4 m/s, 20.1 m/s, 23.2 m/s, and 25.8 m/s). The material of the pressure bar was maraging steel (18Ni). The impact speed was measured by an infrared velocimeter (Lightsensing, Beijing, China), and its response time was 25 μs. The schematic diagram and physical photos of the self-built SHPB experimental device are shown in Figure 2. The control of the impact speed was realized by changing the speed ( $v$ ) of the striker bar by adjusting the air pressure. With the increase in impact speed, the deformation strain rate and impact force of the specimen would increase until the specimen broke. In the experiment, the strain signal was measured by the strain gauge pasted on the bar, and the sensitivity coefficient of the strain gauge was 1.94. The model of the super dynamic strain instrument was SDY2107B (Bdhsd, Beidaihe, China), that of the acquisition card was USB12047 (Bdhsd, Beidaihe, China), and that of the bridge box was SDY2301 (Bdhsd, Beidaihe, China).

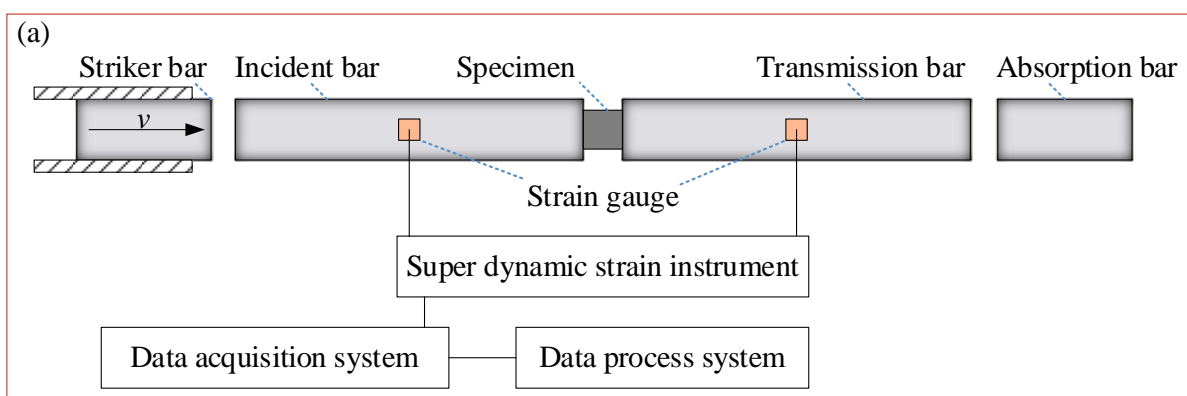


**Figure 2.** Cont.

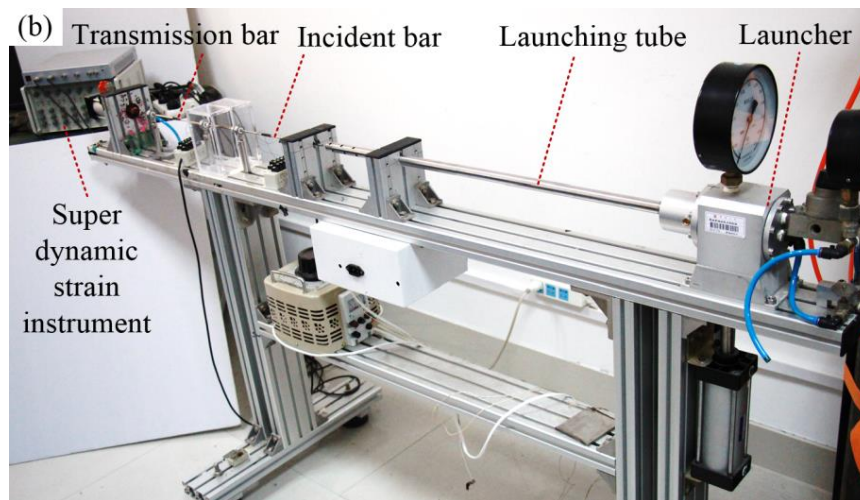


**Figure 2.** (a) Schematic diagram of the SHPB experimental device; (b) photograph of the SHPB experimental device.

The incident, reflected, and transmitted signals in the SHPB experiment of 45CrNiMoVA steel are shown in Figure 3. The specimens were deformed by only one stress pulse before fracture; hence, the surface morphology after fracture was generated after only one stress pulse.

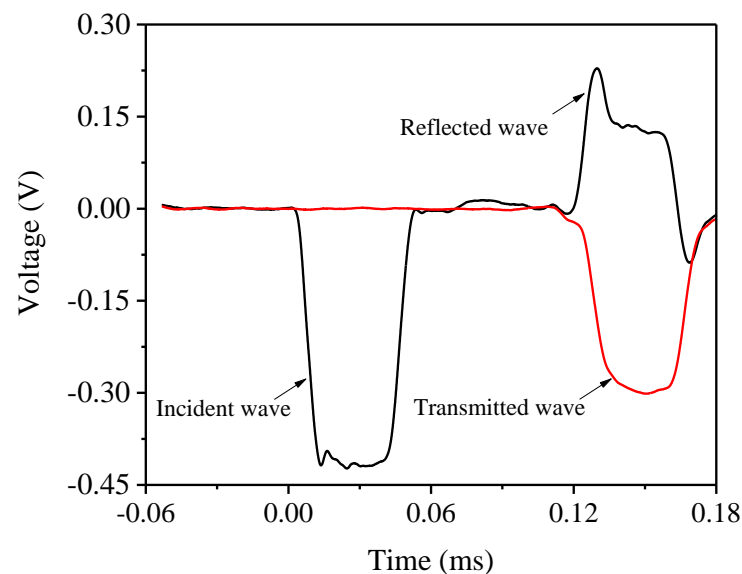


**Figure 3.** The signals of incident, reflected, and transmitted wave of 45CrNiMoVA steel in the SHPB experiment.

The reflected and transmitted waves reflected the deformation information of the specimen under impact loading. According to Equations (1)–(5), the true stress ( $\sigma_T$ )–true strain ( $\epsilon_T$ ) curves of the specimens at different strain rates were obtained. The specimen was cylindrical, with a diameter of 2 mm and an aspect ratio of 1, as shown in Figure 4a. The surface of the specimen was turned. The roughness of the end face was  $Ra$  0.701, and that of the cylindrical surface was  $Ra$  1.571, as shown in Figure 4b,c, respectively.

$$\sigma(t) = E \left( \frac{A}{A_s} \right) \epsilon_t(t) \quad (1)$$

$$\varepsilon(t) = -2 \frac{C_0}{L} \int_0^t \varepsilon_r(\tau) d\tau \quad (2)$$

$$\dot{\varepsilon}(t) = -2C_0\varepsilon_r(t)/L_s \quad (3)$$

$$\sigma_T = (1 - \varepsilon(t))\sigma(t) \quad (4)$$

$$\varepsilon_T = -\ln(1 - \varepsilon(t)) \quad (5)$$

Here,  $C_0$  is the speed of the one-dimensional elastic wave in pressure bar ( $5 \times 10^3$  m/s);  $L_s$  is the length of the specimen;  $\varepsilon_r$  is the strain in the incident bar by the reflected wave;  $\varepsilon_t$  is the strain in the transmission bar by the transmitted wave;  $E$  is the elasticity modulus of the bar (190 GPa); and  $A$  and  $A_s$  are the cross-sectional area of the bar and the specimen, respectively.

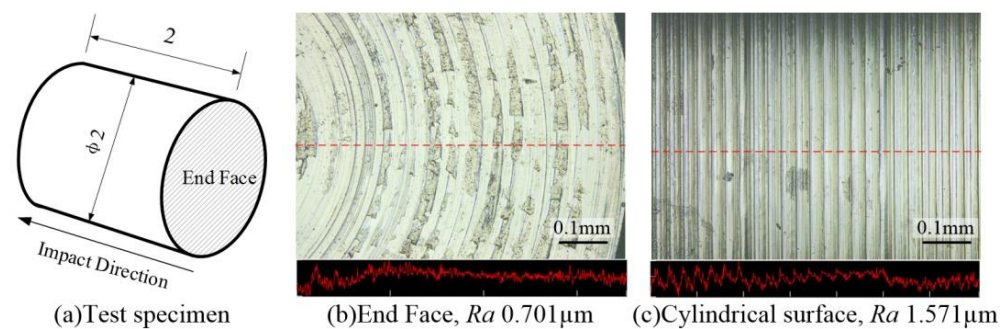


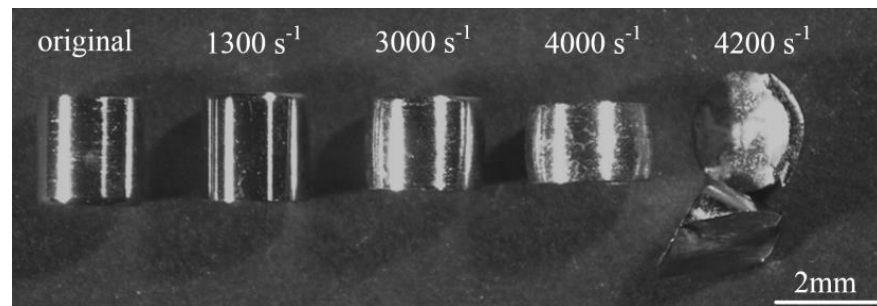
**Figure 4.** Specimen size and surface topography for the SHPB test. (a) Impact-loaded cylindrical specimen size, unit: mm; (b) machined morphology of the end face of the specimen and its two-dimensional line profile; (c) machined morphology of the cylindrical surface of the specimen and its two-dimensional line profile.

After impact loading, we polished and etched the cross section parallel to the axis of the deformed specimen to observe the deformation of the microstructure and possible microcracks. The mass of the etchant solution was composed of 4% nitric acid and 96% ethanol, and the etching time was about 15 s. The fractured specimen was cleaned by an ultrasonic cleaner (KQ-300VDB, Kunshan, China) in absolute ethanol to observe the surface morphology of the fracture. The microstructural evolution of the specimen after deformation and fracture was observed by a laser scanning microscope (LSM, VK-X100, Keyence Corporation, Osaka, Japan) and a scanning electron microscope (SEM, Quanta 650 FEG, FEI Company, Hillsboro, OR, USA), and the deformation, crack propagation, and fracture characteristics under impact loading were analyzed. The grain size of the microstructure of the specimen matrix was measured by electron backscattered diffraction (EBSD), and the acceleration voltage was 20 kV. The surface roughness ( $Ra$ ) was measured from the surface topography collected by the LSM.

### 3. Results and Analysis

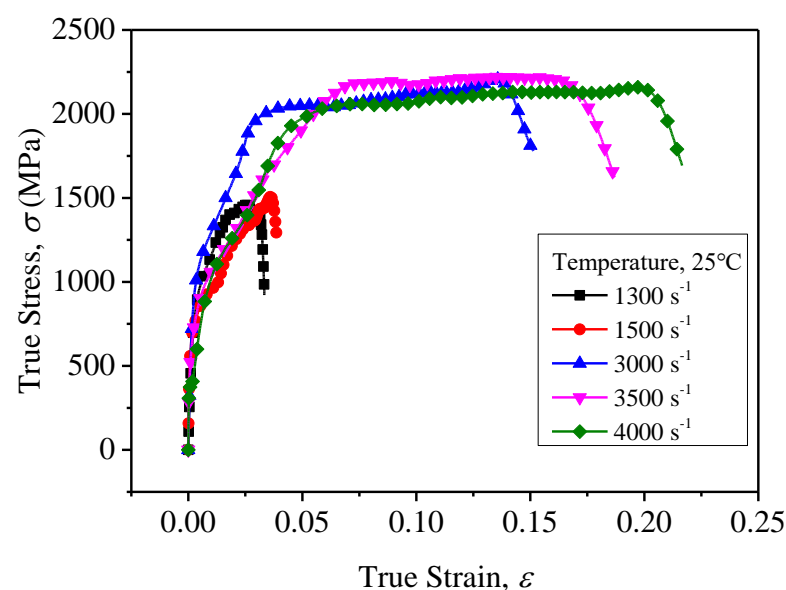
#### 3.1. Severe Plastic Deformation

Figure 5 shows the original and retrieved 45CrNiMoVA steel specimens. The retrieved specimens were obtained at different impact loading speeds, with strain rates of  $1300 \text{ s}^{-1}$ ,  $3000 \text{ s}^{-1}$ ,  $3500 \text{ s}^{-1}$ , and  $4000 \text{ s}^{-1}$ , respectively, and the corresponding strains were 0.033, 0.151, 0.217, and 0.251, respectively. Under small strain, 45CrNiMoVA steel specimen breaks, which reflects the mechanical characteristics of low fracture toughness and weak, cold plastic deformation ability, which is related to the brittleness of martensite structure.



**Figure 5.** The original and retrieved 45CrNiMoVA steel specimens after impact loading.

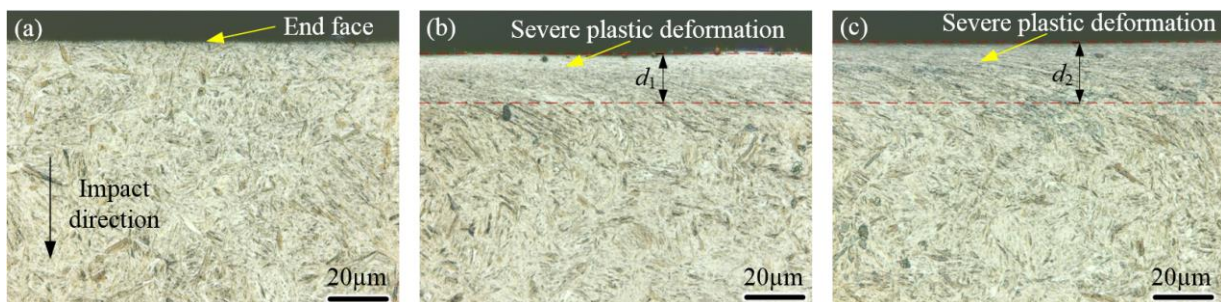
The true stress–true strain curves of the specimen under different strain rates were measured, as shown in Figure 6. When the strain rate was 1300 s<sup>-1</sup> and 1500 s<sup>-1</sup>, the impact-loading speed was relatively low, and the deformation of the specimen was small and mainly elastic deformation. With the increase in the impact speed, the deformation of specimen increased, and the plastic deformation began to play a larger role. At the strain rates of 3000 s<sup>-1</sup>, 3500 s<sup>-1</sup>, and 4000 s<sup>-1</sup>, the true stress–true strain curve showed an obvious flow stress stage, and the ultimate compressive strength exceeded 2000 MPa, which is close to the SHPB experimental results of Hu et al. [5]. In addition to strain hardening, the deformation under impact loading also involved the adiabatic temperature rise effect caused by the high strain rate. The high temperature formed by the adiabatic temperature rise promoted dynamic recovery and dynamic recrystallization during deformation, which is the main reason for strain softening. When strain hardening and strain softening reached a balance, the flow stress stage in the true stress–true strain curve was characterized by stability, which is the reason the flow stress in Figure 6 appears stable and without vibration. Although dynamic recovery and dynamic recrystallization are the key mechanisms of strain softening, there are still differences in the influence of the microstructures between them. According to Sakai et al. [29], dynamic recrystallization usually occurs under large strain, and its flow stress stage curve often shows fluctuations with obvious peaks rather than stationary characteristics. Therefore, the main softening mechanism of 45CrNiMoVA steel specimen under impact loading is dynamic recovery, and dynamic recrystallization is still difficult to obtain under this condition.



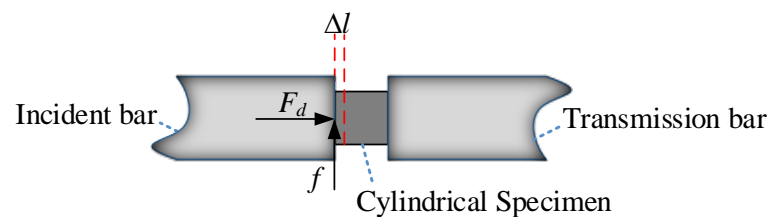
**Figure 6.** The true stress–true strain curves of 45CrNiMoVA specimens under different strain rates.

Figure 7 shows the microstructure near the end face of the cylindrical specimen with different strain levels and strain rates. Under the deformation condition of a relatively

low strain rate ( $1300 \text{ s}^{-1}$ ), the microstructure morphology of the near surface layer of the specimen is shown in Figure 7a. Under the deformation conditions of a high strain rate ( $3000 \text{ s}^{-1}$  and  $4000 \text{ s}^{-1}$ ), as shown in Figure 7b,c, the microstructure of the near surface layer of the specimen formed an obvious local plastic deformation layer with a depth of about  $20\text{--}30 \text{ }\mu\text{m}$ . Under impact loading, the end face of the cylindrical specimen was directly impacted. The high strain rate led to the specimen not having enough time to complete plastic deformation, and the deformation between grains was uneven. The near surface layer material absorbed most of the impact energy and formed this local deformation layer. With the increase in impact load, the deformation layer was likely to change into the ASB and became the most vulnerable area of the specimen. The formation of the inclined arrangement of martensitic laths in the deformed layer was related to the manner of impact loading. The impact force caused friction between the end face of the incident bar and the end face of the specimen. Figure 8 shows the impact force ( $F_d$ ) and friction force ( $f$ ) on the end face of the cylindrical specimen under impact loading. Owing to the friction effect of the end face, the area near the cylindrical end face would produce an uneven deformation area with a width of  $\Delta l$ . Axial stress ( $\sigma$ ) and shear stress ( $\tau$ ) were caused by end friction in the nonuniform deformation area, while only axial stress ( $\sigma$ ) existed in the inner uniform deformation area.



**Figure 7.** The microstructure of the near-end surface of the cylindrical specimen after different impact-loading speeds. (a) The strain was about 0.033, and the strain rate was about  $1.3 \times 10^3 \text{ s}^{-1}$ ; (b) the strain was about 0.151, and the strain rate was about  $3 \times 10^3 \text{ s}^{-1}$ ,  $d_1$  is the thickness of local deformation layer; (c) the strain was about 0.217, and the strain rate was about  $4000 \text{ s}^{-1}$ ,  $d_2$  is the thickness of local deformation layer.



**Figure 8.** In the process of impact loading, the end face of the cylindrical specimen bore the impact force ( $F_d$ ) and friction force ( $f$ ) brought by the end face of the incident bar.

### 3.2. Cracks

The combination of the near-end deformation layer and the notch left by the end surface machining magnified the effect of stress concentration, resulting in the formation of microcracks in the deformation area, as shown in Figure 9. (The white broken line is the axis of the cylindrical specimen.) One main crack and several microcracks were found in the near-end face layer of the specimen, and all of them originated from the end face. In contrast, the deformation layer near the end face of the specimen here was caused by impact loading, not the defect of the material itself. Therefore, in addition to the influence of the surface integrity of the structure on the crack formation, it is necessary to pay attention to the deformation caused by the impact-loading process, especially the local uneven severe

deformation. The morphology and distribution of the deformed grains showed that the shear localization was the result of grain rotation and rearrangement. Chen [30] posited that although there is a large shear strain in the shear band, the formation of microcracks is restrained by high hydrostatic pressure. However, when the shear band is combined with the stress concentration, the crack may be induced more easily. In Figure 9b, it can be observed that the propagation direction of the initial microcrack and the main crack in the deformed layer was consistent with the arrangement direction of the deformed martensitic lath (Figure 9c). The growth of microcracks in the deformation layer stopped, which shows that the crack propagation resistance was large. With the disappearance of the deformed layer, the main crack deflected, and the crack growth was not a direction-dependent occurrence. Owing to insufficient external impact, the main crack stopped growing in the stable growth stage (Figure 9d).

In the deformation zone, the crack had the minimum propagation resistance along the martensite arrangement direction, and the martensite gap became the main propagation path to avoid excessive martensite fracture. However, the main crack growth outside the deformation zone no longer had obvious directionality because of the free arrangement of martensite. This kind of martensite gap could also be found clearly in Zhang's [31] study. Although the crack growth path in the deformation zone looked more like brittle fracture, a straight feature, no further expansion of microcracks indicates that this was not a simple brittle fracture, as the crack tip was still affected by the grain boundary and grain orientation stress. Under impact loading, the inhomogeneous plastic deformation of the specimen affected its energy storage, the martensitic lath gap was squeezed to the limit, and the crack growth led to energy release. Dekhtyar et al. [32] found that micropore healing occurred in the deformed layer, which hindered the crack growth.

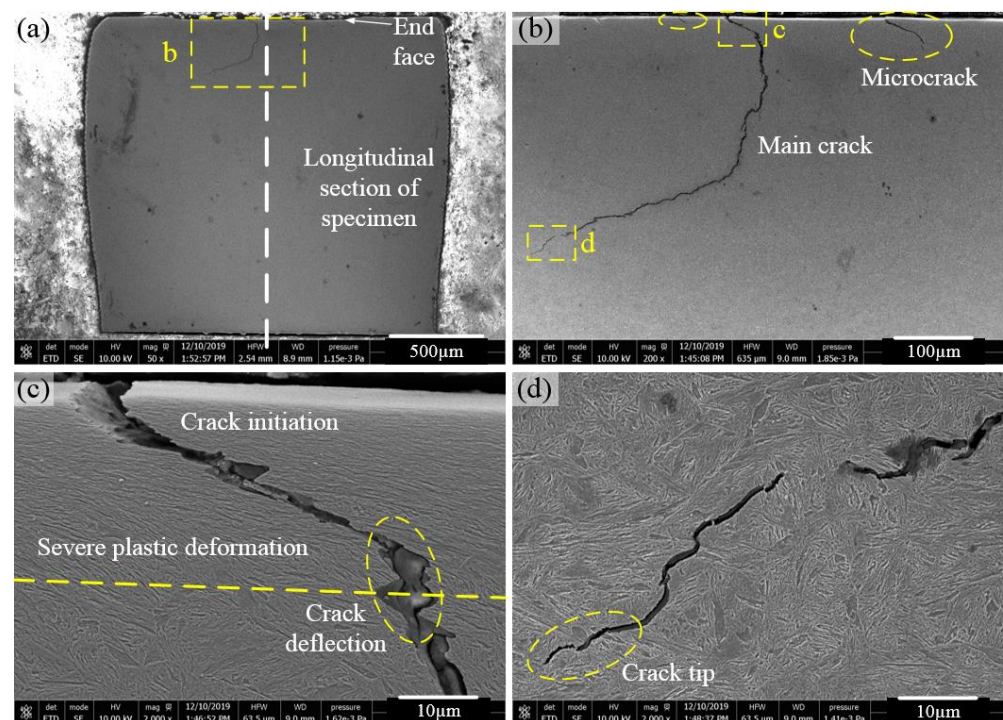


**Figure 9.** Local deformation layer and crack of the 45CrNiMoVA steel specimen after impact loading had a strain rate of about  $4 \times 10^3 \text{ s}^{-1}$ : (a) the whole specimen section; (b) microcracks and main crack, a local enlargement of the area b in the yellow square in the figure (a), the yellow circle is microcrack; (c) local deformation layer and main crack, a local enlargement of the area c in the yellow square in the figure (b), the main crack deflection occurs at the yellow circle; (d) main crack tip, a local enlargement of the area d in the yellow square in the figure (b), the yellow circle is the crack tip.

### 3.3. Fracture

Under impact loading, the cylindrical specimen first underwent upsetting deformation (Figure 10b). With the increase in impact speed, the specimen broke (Figure 10c). Shear fracture was the main fracture form of the cylindrical specimen. The fractured specimen was divided into two pieces, as shown in Figure 11a,d, respectively. Based on the observation of the two matched fracture morphologies, the crack propagation mechanism of 45CrNiMoVA steel under impact loading was analyzed.

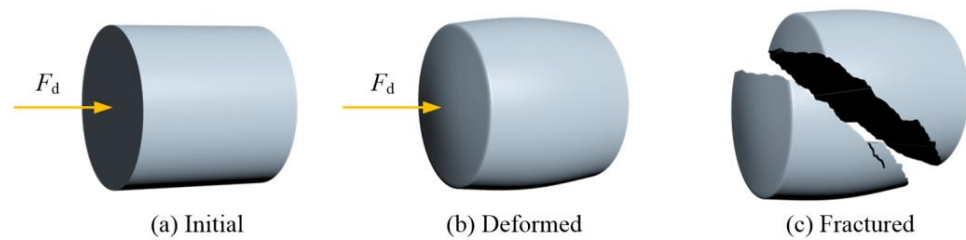


**Figure 10.** Failure process diagram of the 45CrNiMoVA steel cylindrical specimen during the SHPB test. (a) Initial state of specimen, (b) Deformed specimen, (c) Fractured specimen.

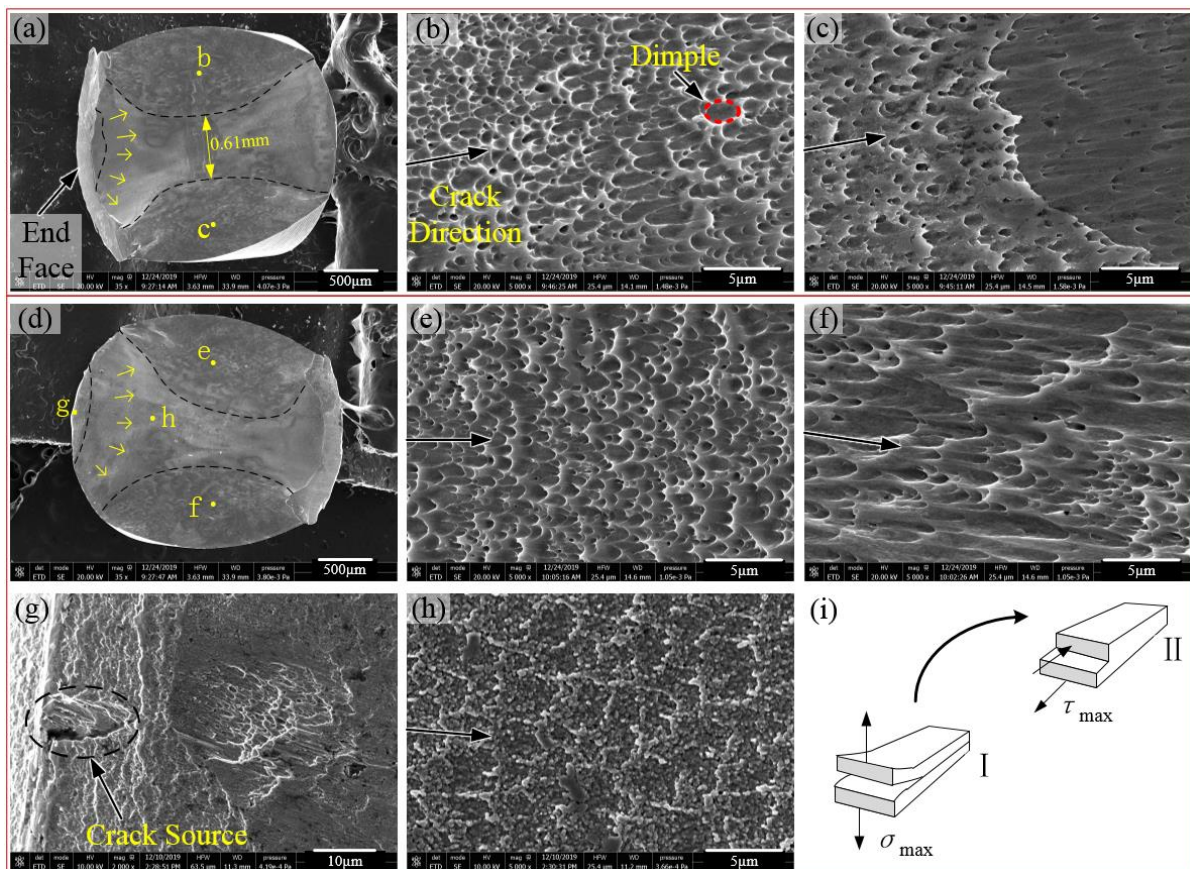


**Figure 11.** Typical impact fracture morphology of 45CrNiMoVA steel, figures (b), (c), (e), (f), (g) and (h) are enlarged from the marks in figures (a) and (d), respectively, the arrow on the fracture surface indicates the direction of crack propagation: (a,d) are two matching macro fractures; (b,e) are the matched shear lip morphologies; (c,f) are the matched shear lip morphologies on the other side; (g) is the morphology the fiber region; (h) is the morphology the radiation region; (i) is the change of the crack propagation stress state, the stress controlling crack growth changes from normal tensile stress to shear stress.

Four areas formed on the macro fracture surface, as shown in Figure 11d, including the fiber region (Figure 11g), radiation region (Figure 11h), and two shear lips (Figure 11e,f). Figure 11g shows the typical fracture morphology of the fiber region, occupying a small area and being located in the near-end surface layer, including the local severely deformed layer and the crack source. The stress concentration at the surface notch led to the crack origin, and machining was the cause of the notch. In this region, the crack originated and then began to grow stably. The low-speed crack growth led to the formation of fibrous morphology, while the local severe deformation led to the existence of high dislocation density and large residual compressive stress, which hindered the crack growth. The crack growth in this stage was controlled by strain. Pavan et al. [33] found that the crack growth rate in the laser impact region was significantly reduced owing to the residual compressive stress caused by deformation. Wang et al. [34] revealed that the gradient structure and residual stress would affect the plastic zone at the crack tip in the process of crack growth, and the residual compressive stress would lead to smaller plastic deformation at the crack tip. They also showed that the deformation layer near the end face could restrain the crack growth.

The crack propagated across the deformation affected zone and then entered the radiation region. Figure 11h is the typical morphology of radiation region. It is a quasi-cleavage fracture, which is between a brittle fracture and ductile fracture. The equiaxed morphology is usually formed under the action of normal stress ( $\sigma_{\max}$ ), which reflects that the crack growth here is mainly affected by normal stress, as shown in crack growth mode I in Figure 11i. Furthermore, the crack growth at this stage was uncontrollable and unstable until fracture. The poor, cold plastic deformation ability of 45CrNiMoVA increased the possibility of brittle fracture. The deformation of the material in the radiation region was extremely small, and the grain boundary and dislocation density had no effect on the crack tip. Because of the high yield strength of the material, the plastic area at the crack tip was extremely small, it was difficult to form passivation at the crack tip, and the stress concentration could not be relieved, which led to the unstable propagation of the crack. The stress at the crack tip exceeded the cleavage fracture strength and formed a cleavage fracture surface. Thompson and Ashby [35] believed that the ductile/brittle fracture of materials is related to the dislocation density at the crack tip. Moreover, Rice and Thomson [36] proposed that crack growth is related to the dislocation emission at the crack tip. The low dislocation density at the crack tip leads to brittle fracture, and the high dislocation density at the crack tip leads to ductile fracture. This indicates that the slow crack propagation rate in the fiber region is related to the high dislocation density in the seriously deformed layer. However, the influence of impact-loading deformation on radiation region was weak, dislocation density was low, and quasi-cleavage fracture occurred. The width ( $b_0$ ) at the center of the radiation region could be used to evaluate the plane strain fracture toughness. According to David [37], plane strain fracture toughness ( $K_P$ ) could be evaluated by Equation (6).

$$\frac{K_Q}{K_P} = \left( 1 + \frac{\delta_f E}{24\sigma_y} \frac{b_0}{b} \right)^{1/2} \quad (6)$$

where  $K_Q$  is the provisional fracture toughness,  $\delta_f$  is the elongation-to-failure measure,  $E$  is the elastic modulus, and  $\sigma_y$  is the yield strength. These parameters are taken from Table 2 as the initial mechanical property parameters of the cylindrical specimen.  $b$  is the maximum possible width of the radiation region, which is 2 mm, and  $b_0$  is the central plane width of the radiation region in Figure 11a, which is 0.61 mm. Based on the width of the central plane of the radiation region, Table 3 shows the plane strain fracture toughness ( $K_P$ ) under impact loading, which was significantly smaller than the initial quasi-static fracture toughness ( $K_Q$ ). It also shows that the formation of radiation region was related to the decrease in fracture toughness under impact loading. Qin et al. [38] compared the influence of the plane width of the central region on plane strain fracture toughness after a pure copper fracture. It was found that the larger  $b_0$  was, the higher  $K_P$  was.

**Table 3.** The plane strain fracture toughness in the radiation region of the fracture surface of 45CrNiMoVA cylindrical specimen.

$\delta_f$ (%)	$E$ (GPa)	$\sigma_y$ (MPa)	$b_0$ (mm)	$b$ (mm)	$K_Q$ (MPa·m <sup>1/2</sup> )	$K_P$ (MPa·m <sup>1/2</sup> )
11	175	1639	0.61	2	41.8	10.48

The shear lip is a typical feature of crack growth in the edge region of the specimen. Under impact loading, the symmetrical shear lip area was formed on the fracture surface of the cylindrical specimen, as shown in Figure 11b,c,e,f. The elongated dimple was the typical fracture surface of the shear lip area. Similar elongated dimple fracture morphology was found in the impact test of martensitic steel by Ghomi and Odeshi [15]. Under the action of an external force, the voids between martensitic laths developed into microvoids, which grew to form dimples. Figure 11b,e show the matched dimples, which were elongated in the opposite direction, reflecting that the crack tip was mainly affected by shear stress ( $\tau_{\max}$ ), as shown in crack growth mode II in Figure 11i. Furthermore, compared with the radiation region, in addition to the different types of stress control, the formation of the shear lip was accompanied by weak strain, while the fiber region was mainly controlled by strain, which constituted the impact fracture characteristics of 45CrNiMoVA.

The shape and size of the dimple in the shear lip can reflect the characteristics of ductile fracture. Stüwe [39] proposed Equation (7) to determine the fracture toughness based on the energy required to form the dimple fracture.

$$K_C \approx \sqrt{\frac{\sigma h_o E}{2}} \quad (7)$$

$$h_o = B d_o \quad (8)$$

where  $K_C$  is the plastic fracture toughness of the shear lip;  $\sigma$  is the average flow stress, which is taken from the maximum stress value in the true stress–true strain curve at a high strain rate;  $h_o$  is the dimple depth;  $E$  is the elastic modulus, from the true stress–true strain curve at a high strain rate; and  $d_o$  is the dimple diameter, from the red circle in Figure 11b. Generally,  $B$  was 0.5, because the dimple observed on the fracture surface was elongated, so  $B$  was taken as 1, and the dimple depth ( $h_o$ ) was calculated according to the dimple diameter ( $d_o$ ). Table 4 shows the fracture toughness results based on the impact fracture dimple morphology.

**Table 4.** Dimple size and fracture toughness of shear lip on the fracture surface of 45CrNiMoVA cylindrical specimen.

$\dot{\epsilon}$ (s <sup>−1</sup> )	$\sigma$ (MPa)	$h_o$ (μm)	$E$ (GPa)	$d_o$ (μm)	$B$	$K_C$ (MPa·m <sup>1/2</sup> )	$K_{IC}$ (MPa·m <sup>1/2</sup> )
>4000	2161	2.17	236.8	2.17	1	23.56	41.8

Compared with the quasi-static fracture toughness ( $K_{IC}$ ), the impact fracture toughness ( $K_C$ ) based on dimple was reduced by 43.6%. Srinivasan et al. [40] proposed that the micro toughness size effect in ductile fracture seems to be related to the dimple height and the material length scale. Considering that the size effect in the micro toughness is important to accurately determine the overall crack growth resistance, in Figure 1b, the grain size of the specimen and the dimple size formed by impact fracture were within an order of magnitude—that is, the effect of micro toughness size should be considered in the process of crack growth. Therefore, the fracture toughness based on the local dimple may only reflect the crack growth resistance of the shear lip. Both the plane strain fracture toughness and the dimple-based fracture toughness of the cylindrical specimens decreased under impact loading. Therefore, 45CrNiMoVA ultrahigh-strength steel structures must avoid surface defects, machining damage, and stress concentration to ensure their safety in the dynamic load service environment.

#### 4. Conclusions

Based on the SHPB test, the deformation and fracture of 45CrNiMoVA steel under impact loading were analyzed, and the following conclusions were obtained:

- (1) Under the condition of high-strain-rate ( $10^3 \text{ s}^{-1}$ ) deformation, the plastic flow stress of 45CrNiMoVA steel shows the characteristics of an equilibrium of strain hardening and strain softening. Near the impact-loading end face, the 20–30  $\mu\text{m}$ -thick local severe plastic deformation layer is an important reason for crack initiation and propagation. The parts should not be subjected to the combination of forward loading and shear loading at the same time. This complex loading environment may lead to the early failure of the parts.
- (2) The fracture morphology of 45CrNiMoVA steel under impact loading consists of a strain-controlled fiber region, normal-stress-controlled quasi-cleavage radiation region, and shear-stress-controlled ductile shear lip. In the study, the impact fracture toughness was reduced by 43.6%, which could lead to quasi-cleavage fracture; hence, this must be paid attention to in the process of material preparation, part design, and manufacturing. It is necessary to avoid introducing surface damage during machining, which may accelerate the failure of parts.

**Author Contributions:** Conceptualization, S.X. and X.L.; methodology, S.X, X.L. and Z.L.; software, X.L.; validation, X.L., Y.D. and S.X; formal analysis, S.X.; investigation, X.L.; resources, X.W.; data curation, S.X.; writing—original draft preparation, X.L.; writing—review and editing, Z.L.; visualization, X.L.; supervision, T.Z. and Y.D.; project administration, Z.L.; funding acquisition, X.W. All authors have read and agreed to the published version of the manuscript.

**Funding:** This work was supported by the National Key R&D Program of China (2019YFB1311100), the Industrial Technology Development Program of China (No. JCKY2021208B046), Advanced Research Foundation of China (No. 80923010501), and the National Natural Science Foundation of China (No. 51975053).

**Data Availability Statement:** The data presented in this study are available on request from the corresponding author.

**Acknowledgments:** Thank Huaqiao University and Beijing North Vehicle Group Corporation for their support for the tests and specimen materials in this paper.

**Conflicts of Interest:** The authors declare no conflict of interest.

#### References

1. Guo, P.; Deng, L.; Wang, X.Y.; Li, J.J. Modelling of dynamic recrystallization kinetics of 300M steel at high strain rates during high deformation. *Sci. China Technol. Sci.* **2019**, *62*, 1534–1544. [[CrossRef](#)]
2. Pokrovskii, A.M.; Dubin, D.A.; Vdovin, D.S. Fatigue–Crack Propagation in Torsional Shafts within the Suspension of High-Speed Caterpillar Vehicles. *Russ. Eng. Res.* **2019**, *39*, 548–555. [[CrossRef](#)]
3. Zhu, S.; Liu, Q.; Peng, W.; Zhang, X. Computational-experimental approaches for fatigue reliability assessment of turbine bladed disks. *Int. J. Mech. Sci.* **2018**, *142*, 502–517. [[CrossRef](#)]
4. Magliaro, J.; Altenhof, W. Energy absorption mechanisms and capabilities for magnesium extrusions under impact. *Int. J. Mech. Sci.* **2020**, *179*, 105667. [[CrossRef](#)]
5. Hu, X.; Xie, L.; Gao, F.; Xiang, J. On the Development of Material Constitutive Model for 45CrNiMoVA Ultra-High-Strength Steel. *Metals* **2019**, *9*, 374. [[CrossRef](#)]
6. Guo, F.; Fei, Q.; Zhang, P.; Li, Y.; Gupta, N. Dynamic shear fracture behaviors and “pseudo-plastic” constitutive model of carbon/carbon composite pins. *Int. J. Mech. Sci.* **2020**, *187*, 105903. [[CrossRef](#)]
7. Qin, H.; Tang, X.Y.; Yao, W.Q.; Wu, F.Q. Fracture and Failure Mechanism Analysis of the 45CrNiMoVA Gear. *Key Eng. Mater.* **2016**, *723*, 349–353. [[CrossRef](#)]
8. Rakvag, K.G.; Boervik, T.; Westermann, I.; Hopperstad, O.S. An experimental study on the deformation and fracture modes of steel projectiles during impact. *Mater. Des.* **2013**, *51*, 242–256. [[CrossRef](#)]
9. Yang, X.; Zhang, B. Material embrittlement in high strain-rate loading. *Int. J. Extreme Manuf.* **2019**, *1*, 022003. [[CrossRef](#)]
10. Zhang, B.; Yin, J. The “skin effect” of subsurface damage distribution in materials subjected to high-speed machining. *Int. J. Extreme Manuf.* **2019**, *1*, 012007. [[CrossRef](#)]

11. Liu, B.; Guedes Soares, C. Effect of strain rate on dynamic responses of laterally impacted steel plates. *Int. J. Mech. Sci.* **2019**, *160*, 307–317. [[CrossRef](#)]
12. Wang, B.; Liu, Z.; Su, G.; Song, Q.; Ai, X. Investigations of critical cutting speed and ductile-to-brittle transition mechanism for workpiece material in ultra-high speed machining. *Int. J. Mech. Sci.* **2015**, *104*, 44–59. [[CrossRef](#)]
13. Hu, D.; Meng, K.; Jiang, H. Experimental Investigation of Dynamic Properties of AerMet 100 Steel. *Procedia Eng.* **2015**, *99*, 1459–1464. [[CrossRef](#)]
14. Singh, N.K.; Cadoni, E.; Singha, M.K.; Gupta, N.K. Dynamic Tensile and Compressive Behaviors of Mild Steel at Wide Range of Strain Rates. *J. Eng. Mech.* **2013**, *139*, 1197–1206. [[CrossRef](#)]
15. Ghomi, H.M.; Odeshi, A.G. The effects of microstructure, strain rates and geometry on dynamic impact response of a carbon–manganese steel. *J. Mater. Sci. Eng. A* **2012**, *532*, 308–315. [[CrossRef](#)]
16. Ren, J.; Xu, Y.; Zhao, X.; Zhao, P. Dynamic mechanical behaviors and failure thresholds of ultra-high strength low-alloy steel under strain rate 0.001/s to 106/s. *J. Mater. Sci. Eng. A* **2018**, *719*, 178–191. [[CrossRef](#)]
17. Harding, I.; Mouton, I.; Gault, B.; Kumar, K.S. Microstructural Evolution in an Fe-10Ni-0.1C Steel During Heat Treatment and High Strain-Rate Deformation. *Metall. Mater. Trans. A* **2020**, *51*, 5056–5076. [[CrossRef](#)]
18. Hao, Y.; Liu, J.; Li, J.; Li, S.; Wang, G. Investigation on dynamic properties and failure mechanisms of Ti-47Al-2Cr-2Nb alloy under uniaxial dynamic compression at a temperature range of 288 K–773 K. *J. Alloys Compd.* **2015**, *649*, 122–127.
19. Nesterenko, V.F.; Meyers, M.A.; LaSalvia, J.C.; Bondar, M.P.; Chen, Y.J.; Lukyanov, Y.L. Shear localization and recrystallization in high-strain, high-strain-rate deformation of tantalum. *J. Mater. Sci. Eng. A* **1997**, *229*, 23–41. [[CrossRef](#)]
20. Krüger, L.; Schwarz, F.; Martin, U.; Roven, H.J. Strain rate and temperature effects on the flow behavior and microstructure of X2CrNiMoN22-5-3 duplex stainless steel. *J. Mater. Sci. Eng. A* **2014**, *592*, 6–11. [[CrossRef](#)]
21. Zhao, W.; Liu, D.; Chiang, R.; Qin, H.; Zhang, X.; Zhang, H.; Liu, J.; Ren, Z.; Zhang, R.; Doll, G.L.; et al. Effects of ultrasonic nanocrystal surface modification on the surface integrity, microstructure, and wear resistance of 300M martensitic ultra-high strength steel. *J. Mater. Process. Technol.* **2020**, *285*, 116767. [[CrossRef](#)]
22. Zhao, W.; Liu, D.; Zhang, X.; Zhou, Y.; Zhang, R.; Zhang, H.; Ye, C. Improving the fretting and corrosion fatigue performance of 300M ultra-high strength steel using the ultrasonic surface rolling process. *Int. J. Fatigue* **2019**, *121*, 30–38. [[CrossRef](#)]
23. Qi, X.; Du, L.; Dong, Y.; Misra, R.D.K.; Du, Y.; Wu, H.; Gao, X. Fracture toughness behavior of low-C medium-Mn high-strength steel with submicron-scale laminated microstructure of tempered martensite and reversed austenite. *J. Mater. Sci.* **2019**, *54*, 12095–12105. [[CrossRef](#)]
24. Das, A.; Chowdhury, T.; Tarafder, S. Ductile fracture micro-mechanisms of high strength low alloy steels. *Mater. Des. (1980–2015)* **2014**, *54*, 1002–1009. [[CrossRef](#)]
25. Gronostajski, Z.; Niechajowicz, A.; Kuziak, R.; Krawczyk, J.; Polak, S. The effect of the strain rate on the stress–strain curve and microstructure of AHSS. *J. Mater. Process. Technol.* **2017**, *242*, 246–259. [[CrossRef](#)]
26. Khodabakhshi, F.; Farshidianfar, M.H.; Gerlich, A.P.; Nosko, M.; Trembosova, V.; Khajepour, A. Microstructure, strain-rate sensitivity, work hardening, and fracture behavior of laser additive manufactured austenitic and martensitic stainless steel structures. *Mater. Sci. Eng. A* **2019**, *756*, 545–561. [[CrossRef](#)]
27. Wang, B.; Duan, Q.Q.; Zhang, P.; Zhang, Z.J.; Li, X.W.; Zhang, Z.F. Investigation on the cracking resistances of different ageing treated 18Ni maraging steels. *Mater. Sci. Eng. A* **2020**, *771*, 138553. [[CrossRef](#)]
28. Chen, F.; Zhang, Y.; Lv, X.; Ma, D. Determination of dynamic fracture toughness of 45CrNiMoVA steel. *Ordnance Mater. Sci. Eng.* **1990**, *01*, 13–18.
29. Sakai, T.; Belyakov, A.; Kaibyshev, R.; Miura, H.; Jonas, J.J. Dynamic and post-dynamic recrystallization under hot, cold and severe plastic deformation conditions. *Prog. Mater. Sci.* **2014**, *60*, 130–207. [[CrossRef](#)]
30. Chen, Z.H.; Chan, L.C.; Lee, T.C.; Tang, C.Y. An investigation on the formation and propagation of shear band in fine-blanking process. *J. Mater. Process. Technol.* **2003**, *138*, 610–614. [[CrossRef](#)]
31. Zhang, Y.; Zhan, D.; Qi, X.; Jiang, Z. Effect of tempering temperature on the microstructure and properties of ultrahigh-strength stainless steel. *J. Mater. Sci. Technol.* **2019**, *35*, 1240–1249. [[CrossRef](#)]
32. Dekhtyar, A.I.; Mordyuk, B.N.; Savvakina, D.G.; Bondarchuk, V.I.; Moiseeva, I.V.; Khripta, N.I. Enhanced fatigue behavior of powder metallurgy Ti–6Al–4V alloy by applying ultrasonic impact treatment. *Mater. Sci. Eng. A* **2015**, *641*, 348–359. [[CrossRef](#)]
33. Pavan, M.; Furfari, D.; Ahmad, B.; Gharghoury, M.A.; Fitzpatrick, M.E. Fatigue crack growth in a laser shock peened residual stress field. *Int. J. Fatigue* **2019**, *123*, 157–167. [[CrossRef](#)]
34. Wang, Y.; Yuan, L.; Zhang, S.; Sun, C.; Wang, W.; Yang, G.; Li, Q.; Wei, Y. The influence of combined gradient structure with residual stress on crack-growth behavior in medium carbon steel. *Eng. Fract. Mech.* **2019**, *209*, 369–381. [[CrossRef](#)]
35. Thompson, A.W.; Ashby, M.F. Fracture surface micro-roughness. *Scr. Mater.* **1984**, *18*, 127–130. [[CrossRef](#)]
36. Rice, J.R.; Thomson, R. Ductile versus brittle behavior of crystals. *Philos. Mag.* **1974**, *29*, 73–97. [[CrossRef](#)]
37. Broek, D. *Elementary Engineering Fracture Mechanics*; Springer: Dordrecht, The Netherlands, 1978.
38. Qin, E.W.; Lu, L.; Tao, N.R.; Tan, J.; Lu, K. Enhanced fracture toughness and strength in bulk nanocrystalline Cu with nanoscale twin bundles. *Acta Mater.* **2009**, *57*, 6215–6225. [[CrossRef](#)]
39. Stüwe, H.P. The work necessary to form a ductile fracture surface. *Eng. Fract. Mech.* **1980**, *13*, 231–236. [[CrossRef](#)]
40. Srinivasan, K.; Huang, Y.; Kolednik, O.; Siegmund, T. The size dependence of micro-toughness in ductile fracture. *J. Mech. Phys. Solids* **2008**, *56*, 2707–2726. [[CrossRef](#)]